

Engineering hyaluronic acid-based nanoassemblies for monoclonal antibody delivery – design, characterization, and biological insights

Ana M. López-Estévez^{1,2,3}, Y. Zhang⁴, María Medel⁵, Iker Arriaga⁶, Lucía Sanjurjo³, Cristian Huck-Iriart⁷, Nicola G. A. Abrescia^{6,8}, María J. Vicent⁵, Defang Ouyang⁴, Dolores Torres², and María José Alonso^{1,2,3} (✉)

¹ Center for Research in Molecular Medicine and Chronic Diseases (CiMUS), University of Santiago de Compostela, Santiago de Compostela 15782, Spain

² Department of Pharmacology, Pharmacy and Pharmaceutical Technology, School of Pharmacy, University of Santiago de Compostela, Santiago de Compostela 15782, Spain

³ Health Research Institute of Santiago de Compostela (IDIS), Santiago de Compostela 15782, Spain

⁴ State Key Laboratory of Quality Research in Chinese Medicine, Institute of Chinese Medical Sciences (ICMS), University of Macau, Macau 999078, China

⁵ Polymer Therapeutics Laboratory and CIBERONC Prince Felipe Research Centre, Valencia E-46012, Spain

⁶ Structure and Cell Biology of Viruses Lab, CIC bioGUNE, Basque Research and Technology Alliance (BRTA), Derio 48160, Spain

⁷ ALBA Synchrotron Light Source, Experiments Division, Cerdanyola del Vallès, Barcelona 08290, Spain

⁸ IKERBASQUE, Basque Foundation for Science, Bilbao 48009, Spain

© The Author(s) 2024

Received: 31 January 2024 / Revised: 3 June 2024 / Accepted: 13 June 2024

ABSTRACT

The current spotlight of cancer therapeutics is shifting towards personalized medicine with the widespread use of monoclonal antibodies (mAbs). Despite their increasing potential, mAbs have an intrinsic limitation related to their inability to cross cell membranes and reach intracellular targets. Nanotechnology offers promising solutions to overcome this limitation, however, formulation challenges remain. These challenges are the limited loading capacity (often insufficient to achieve clinical dosing), the complex formulation methods, and the insufficient characterization of mAb-loaded nanocarriers. Here, we present a new nanocarrier consisting of hyaluronic acid-based nanoassemblies (HANAs) specifically designed to entrap mAbs with a high efficiency and an outstanding loading capacity (50%, w/w). HANAs composed by an mAb, modified HA and phosphatidylcholine (PC) resulted in sizes of ~ 100 nm and neutral surface charge. Computational modeling identified the principal factors governing the high affinity of mAbs with the amphiphilic HA and PC. HANAs composition and structural configuration were analyzed using the orthogonal techniques cryogenic transmission electron microscopy (cryo-TEM), asymmetrical flow field-flow fractionation (AF4), and small-angle X-ray scattering (SAXS). These techniques provided evidence of the formation of core-shell nanostructures comprising an aqueous core surrounded by a bilayer consisting of phospholipids and amphiphilic HA. *In vitro* experiments in cancer cell lines and macrophages confirmed HANAs' low toxicity and ability to transport mAbs to the intracellular space. The reproducibility of this assembling process at industrial-scale batch sizes and the long-term stability was assessed. In conclusion, these results underscore the suitability of HANAs technology to load and deliver biologicals, which holds promise for future clinical translation.

KEYWORDS

monoclonal antibody, nanoparticles, hyaluronic acid, characterization, particle size, computational modeling

1 Introduction

Monoclonal antibody (mAb)-based therapies, extensively employed in clinical settings, represent a breakthrough in oncology [1]. Such success has redirected the focus of cancer therapeutics towards personalized medicine, leveraging the specificity and selectivity of biologicals. Despite the recognized potential of mAbs, challenges such as immunogenicity, limited diffusion across the tumor stroma, and the inability to cross cell membranes to access intracellular oncoproteins have hindered their widespread exploitation [2–4]. In this context, the application of nanotechnology for the delivery of mAbs opens up the possibility to bypass these challenges, enabling mAbs to reach

intracellular targets, a field still barely explored [5, 6]. However, challenges associated with mAb delivery remain mainly unaddressed due to the poor consideration of target disease requirements during NPs design and the complexities associated with specific nanotechnologies [5, 7]. This current status underscores the need for disease-oriented nanocarrier design and a deeper understanding of such products prior to market launch.

Recognizing the multiple biological barriers that NPs potentially encounter during their journey to a target tissue remains crucial for the development of the next generation of oncological treatments [8, 9]. Engineering NPs for precision medicine represents a customizable process with certain generally agreed-upon design parameters. For instance, particle sizes close to or

below 100 nm determine pharmacokinetics and bio-distribution of the NPs [10–12], while neutral and hydrophilic coating surfaces diminish unspecific uptake [13–15] and extend blood circulation times [16, 17]. Surface composition also influences NPs accumulation by modulating protein corona formation [18]. In this sense, PEGylation is the leading strategy as evidenced by the number of PEGylated NPs in the market [19].

In the pursuit of designing NPs with desired attributes, an array of mAb delivery systems, including liposomes [20–23], micelles [24–26], and poly(lactic-glycolic)-based NPs [27–29], have been explored. Interestingly, the majority of nanocarriers have been tailored for delivering the anti-angiogenic mAb Bevacizumab (BVZ) – an mAb that targets vascular endothelial growth factor (VEGF) – under the premise that targeting intra- and extracellular VEGF pools may improve therapeutic responses. Despite the promising features of these delivery systems, there are crucial aspects that need to be addressed to maximize their clinical potential. One of such is the incapacity of some NPs to preserve the active conformation of the mAb [30]. Another critical one is the limited loading capacity of reported nanocarriers, which fall below 10%, w/w [28, 31] and provide inconclusive evidence of their structural organization. Furthermore, crucial pharmaceutical features, such as biological and physical stability during storage have been scarcely reported. The complexity of their formulation methods and the absence of components with a favorable safety profile further accentuate the hurdles faced in their development.

Here we report the development of HA-based hybrid nanoassemblies (HANAs), a delivery system never reported for the delivery of mAbs, in an effort to combine the specific features of polymeric nanoparticles (NPs) and liposomes [32]. The components of HANAs were selected based on their inherent affinity and capacity to enable high loading capacities while preserving the biological activity of the mAb. This selection is made with a dual focus on ensuring the safety profile and simplifying the overall formulation process. In this sense, a highly attractive biomaterial that stands out due to its safety profile and targeting attributes is hyaluronic acid, HA [31, 33]. HA's targeting ability relies on its capacity to recognize CD44 receptors, a glycoprotein overexpressed on several cancers [34, 35], serving as mediator of cell internalization. The incorporation of hydrophobic motifs offers interesting opportunities for tailoring the assembling and structural properties of HA-based nanocarriers [36–39]. To induce the assembling, phosphatidylcholine (PC) was selected, which is commonly employed in liposome production [40].

Following the design of a nanocarrier that fulfills the minimum requirements for the specific application, robust nanomaterial characterization is imperative for the advancement of nanomedicine applications, ensuring reproducibility and successful translation [41, 42]. Significant strides towards this goal are currently being made through collaborative efforts involving researchers, industry, and regulatory agencies, with a particular emphasis on the field of nanotechnology. In response, the National Cancer Institute (NCI) has made efforts to ease the clinical translation of nanotechnologies by providing guidelines for NPs characterization [43]. Similarly, in an effort to standardize reporting in the realm of bio-nanosystems, a set of minimum standards has been proposed (MIRIBEL checklist [44]). Beyond, the risk assessment of nanomaterials having into account the type of material, time of residence in the body, among others, have been recently collected [45].

Building on this background, this study aims to develop a novel nanotechnology for the delivery of mAbs with high possibilities for clinical translation. We hypothesized that mAb entrapment within HANAs will yield high mAb loading. Our first objective encompasses an in depth-characterization and structural

elucidation of the HANAs, while understands the parameters that determine the entrapment of the mAb, secondly, to evaluate their *in vitro* performance in relevant cancer cell lines to discard a toxicity-related failure as well as the capacity to internalize mAbs, and finally, the validation for an industrial production through different scaling-up methodologies.

2 Results and discussion

2.1 Development and physicochemical characterization of HANAS

Our main objective was the rational design and the in-depth-characterization of a novel nanocarrier engineered to overcome challenges associated with mAb delivery, such as the absence of components with a favorable safety profile, the complexity of their formulation methods, insufficient loading capacities, and poor structural characterization. Our design involved the development of a novel delivery system – HANAs – through the combination of two pivotal components – palmitoyl hyaluronate (HAC16) and phosphatidylcholine (Lipoid S100). The rationale behind this design rested on leveraging the hydrophobic domains [46] and net positive charge under physiological conditions [47] of mAbs, which would maximize the interactions with the negatively charged and hydrophobic HA. Furthermore, the incorporation of Lipoid S100, commonly employed in liposome production [40], facilitated the assembling process. Our selection not only enabled the efficient encapsulation of the model mAb, BVZ, a straightforward assembly technique, but also imparted an advantageous regulatory profile to the resultant HANAs (Fig. 1).

Hence, two different amphiphilic HA polymers, HAC16 degree of substitution (DS) 1%–10% and HAC16 DS 10%–15%, were explored for the development of the HANAs, with the idea of studying their impact on particle size. As depicted in Fig. S1 in the Electronic Supplementary Material (ESM), the overall observation was that particle sizes remained below 300 nm, regardless of the DS of the HAC16. Nevertheless, when analyzed in detail, different tendencies became evident. Notably, when increasing concentrations of HAC16 DS 10%–15% and Lipoid S100 were tested, an inverse correlation between the particle size and the amount of polymer was observed, regardless of the lipid. Similar results were subscribed to the HA with lower hydrophobic substitutions (DS 1%–10%), although the number of conditions tested that yielded NPs was inferior. Certainly, the polymer with a greater number of hydrophobic moieties drove the formation of monodisperse NPs with particles sizes ranging from 300 to 200 nm, suggesting the role played by the hydrophobic interactions in the assembling of the HANAs (HA-200, 200 nm, DS 10%–15% vs HA-160, 160 nm, DS 1%–10%). Moreover, these findings allow us to speculate about the role played by the mAb in the assembling dynamics of the HANAs. To validate this hypothesis, the amount of mAb employed for the obtention of the NPs was reduced from 2 to 0.5 mg/mL. Interestingly, the opposite trend from the one stated above was noticed, a direct correlation between the particle size and the amount of Lipoid S100 and polymer, albeit to the latter case. We postulate that the low concentration of materials utilized in this formulation enhances the interaction of the BVZ with the components of the HANAs, leading to final candidate with optimal particle size for tumor accumulation (~ 100 nm) [10–12], so called HA-100.

To further expand the properties of HANAs, they were granted with a stealth corona through the incorporation of PEG to the NPs' surface. To achieve this, varying concentrations of DSPE.PEG_{2K} were tested. As shown in Fig. S2 in the ESM, only a concentration of 0.25 mg/mL (PEGHA-100) preserved the main physicochemical properties of the HANAs, while superior



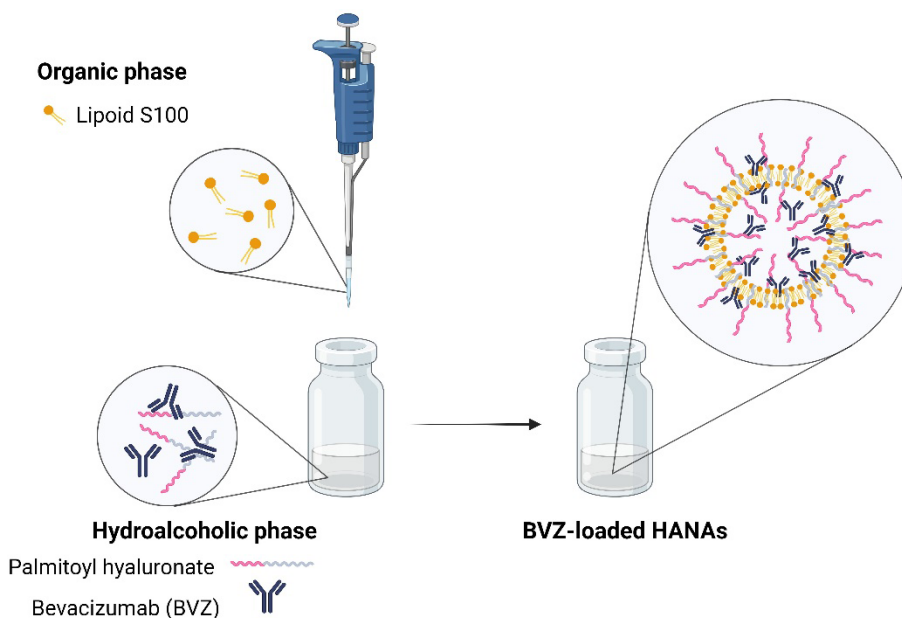


Figure 1 Schematic representation of the formulation method carried out for the development of HANAs. The assembly process involves the preparation of essential components, primarily hyaluronic acid polymer and mAb solutions. These components are carefully mixed in a suitable solvent solution to facilitate uniform dispersion and interaction. Subsequently, the mixture undergoes incubation under controlled conditions and a lipid solution is added to promote self-assembly, leading to the formation of HANAs. The physicochemical properties of the resulting HANAs are determined following the below orthogonal sizing techniques.

amounts led to polydispersity index (PDI) > 0.3. Consequently, the resulting HANAs entrapping BVZ had a particle size within the range of 80–200 nm and neutral surface charge as determined by dynamic light scattering (DLS) and laser Doppler anemometry, respectively (Table 1).

Given the novelty of the HANAs, the utilization of different orthogonal sizing techniques is indispensable as an initial step to comprehend and validate their potential for clinical applications [43, 44]. Thus, nanoparticle tracking analysis (NTA) was conducted. As shown in Fig. 2, NTA analysis corroborated the consistency of the particle size measurements obtained by DLS for HA-160 and PEGHA-100. Larger differences were found for HA-200 and HA-100, which could be related to the NTA goodness for the characterization of heterogeneous populations [48]. NTA distribution parameters and statistical differences were described in detail in Table S1 in the ESM.

2.2 Structural characterization of HANAs by asymmetrical flow field-flow fractionation (AF4) and small-angle X-ray scattering (SAXS)

AF4 has emerged as a valuable tool for characterizing formulations given its ability to profile multiple populations and provide insight into critical quality attributes such as size, shape, and dispersity. This is particularly relevant in the characterization of the HANAs as it allows to identify the non-entrapped BVZ and the BVZ-loaded HANA-160 populations, as have been shown in

the fractograms in Fig. 3(a). The smaller first eluted population may suggest the presence of the mAb, albeit at low concentrations, suggesting high entrapment efficiency. A significant population of HANAs becomes eluted at prolonged retention times. The polydispersity of the sample is proved by the long-eluted tails, following the main peak, which is supported by the average R_g values (R_{g1} : 45 ± 1 , R_{g2} : 53 ± 3 , and R_{g3} : 63 ± 5) [49]. In general, we found smaller size values by AF4-MALS than those obtained by DLS, which may be due to the assumed sphericity or the more intense scattering of light by larger particles [50]. These results suggest the presence of a bilayer structure with an inner core exhibiting a composition distinct from that of the bilayer.

SAXS profiles and corresponding diameter distribution functions revealed apparent 3D conformational differences between empty (blank HA-160) and mAb-loaded HANAs (mAb-loaded HA-160) in solution (Figs. 3(b) and 3(c)). We fitted curves to a multi concentric spherical-shell model [51] to consider a bilayer shell (ca. 4 nm shell thickness), yielding diameter sizes of 40 nm (blank HA-160) and 60 nm (mAb-loaded HA-160), which align with the above-described AF4 values. Moreover, no significant changes were observed in the overall shell thickness. SAXS profiles between blank and mAb-loaded HANAs display broad similarities with the expected curvature. A new contribution to the scattering intensity was observed at medium q-range for mAb loaded HANAs sample. We modeled this contribution with a Guinier-Porod semiempirical form factor [52]. We found an

Table 1 Physicochemical properties of the BVZ-loaded HANA prototypes (final BVZ concentration: 3.2 mg/mL)

Prototype	Final concentration (mg/mL)				Physicochemical properties		
	BVZ	HA C16	Lipoid S100	DSPE. PEG	Particle size (nm)	PDI	Zeta potential (mV)
HA-200 ^a	3.2	2	0.25	-	196 ± 13	0.24	-14 ± 1
HA-160 ^b	3.2	2	1	-	162 ± 17	0.23	-13 ± 2
HA-100 ^b	3.2	1.6	3.2	-	107 ± 14	0.23	-13 ± 3
PEGHA-100 ^b	3.2	1.6	3.2	1.6	79 ± 8	0.25	-13 ± 2

The physicochemical properties were determined by dynamic light scattering (particle size and PDI) and laser Doppler anemometry (Zeta potential). Data are expressed as mean ± SD, $n \geq 3$.

HANA prototypes differ in the degree of substitution (DS): HAC16 DS 10%–15%^a and DS 1%–10%^b.

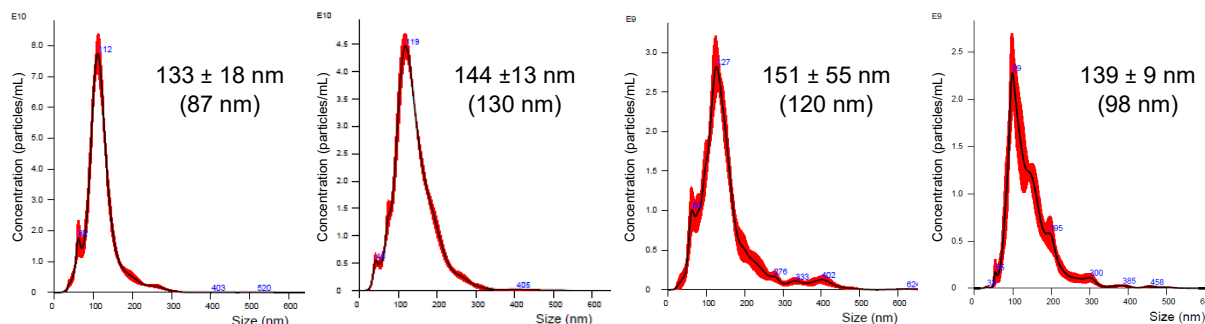


Figure 2 Graphs size distribution of the BVZ-HANAs by NTA. Data are expressed as mean \pm SD (mode), $n \geq 3$.

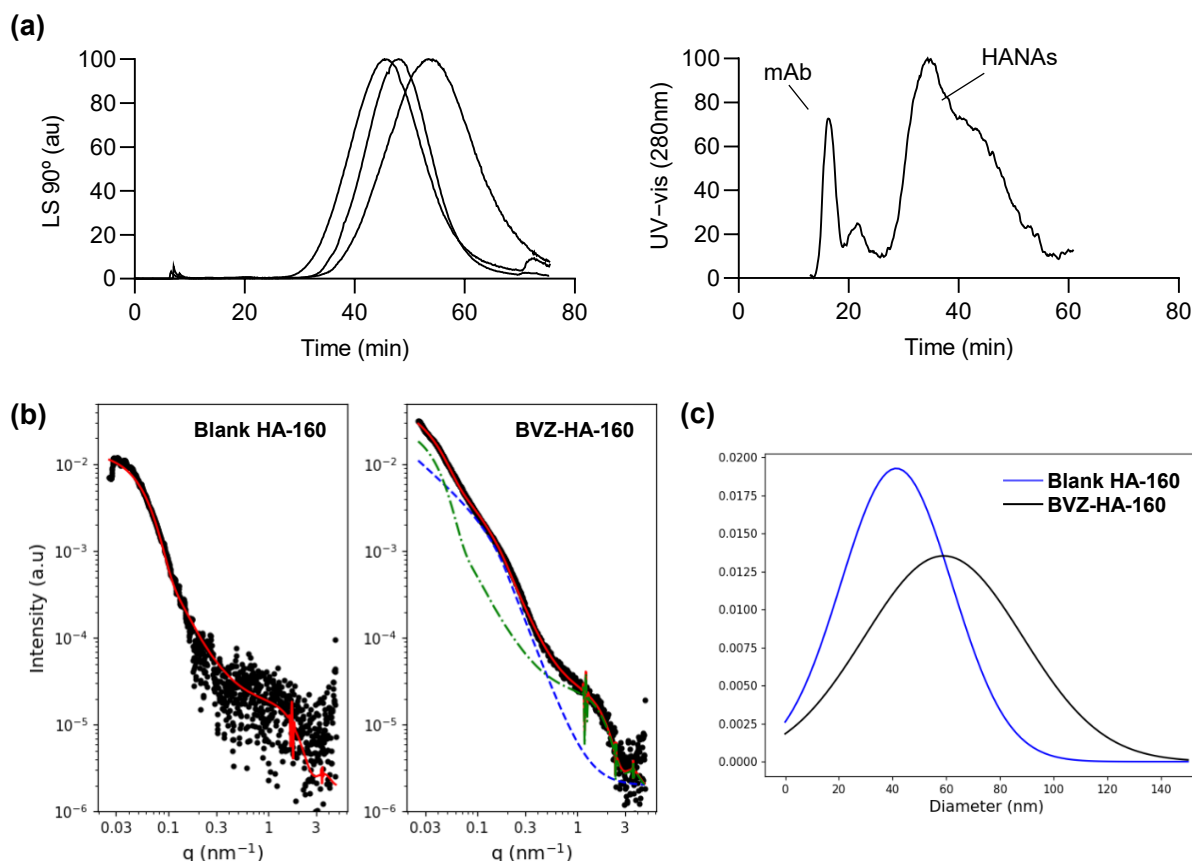


Figure 3 (a) AF4 fractograms of BVZ-HA-160 with a light scattering 90° detector (left graph) and UV-vis signal at 280 nm (right graph). The region corresponding to the mAb and the main HA-160 population were indicated. (b) SAXS profile of blank HA-160 (left) and BVZ-HA-160 (right), and (c) corresponding diameters. In green line, the BVZ-HA-160 forms a factor while an unknown structure is present in the blue line.

estimated diameter of the unknown structure at around 14 nm, which is larger than free BVZ and most probably indicates the formation of a supramolecular structure inside.

Overall, orthogonal sizing techniques validate the hydrodynamic particle size of HANAs and reaffirm their reproducibility, providing essential insights for their potential clinical application.

2.3 The architecture of HANAs by cryogenic transmission electron microscopy (cryo-TEM)

Aiming to study in detail the structures discerned by SAXS, the HANAs with the most pronounced differences (i.e., HA-160 and PEGHA-100) were selected for the characterization of their architectural organization by cryo-TEM as this technique allows to vitrify the NPs in their native state.

In terms of structural organization, the 2D cryo-images indicated the presence of unilamellar vesicles consisting of a lipid/polymer bilayer and an aqueous core, without noticeable differences when the mAb was entrapped into the HANAs (Fig. 4). Besides, the presence of undefined nanostructures was

identified for the BVZ-loaded HANAs, suggesting the self-aggregation of the mAb or the formation of HAC16-BVZ or Lipoid S100-BVZ complexes. To gain insight into the permeability of the bilayer [53], the thickness was determined, estimated to fall within the range of 6–8 nm for PEGHA-100.

Morphological analysis unraveled spherical, oval, as well as tubular-like shapes for HA-160, whereas a predominant spherical shape was inferred for PEGHA-100. These morphological differences may be governed by the steric repulsion provided by the PEG corona of PEGHA-100 [54]. Despite, cryo-TEM images further confirmed the particle size displayed by the above orthogonal sizing techniques. In addition, a particle size distribution histogram of PEGHA-100 by cryo-TEM (Fig. S3 in the ESM) corroborates the results displayed by DLS.

As a whole, on the basis of this structural analysis, we could infer a population of bilayer polymer/lipid assemblies [55, 56] in the presence of irregular undefined aggregates. Following multiple orthogonal high-resolution sizing measurements, we have comprehensively characterized the material structure and its inherent complexity, in accordance with the recent draft regulatory guidance provided by the FDA [57]. Moreover, we

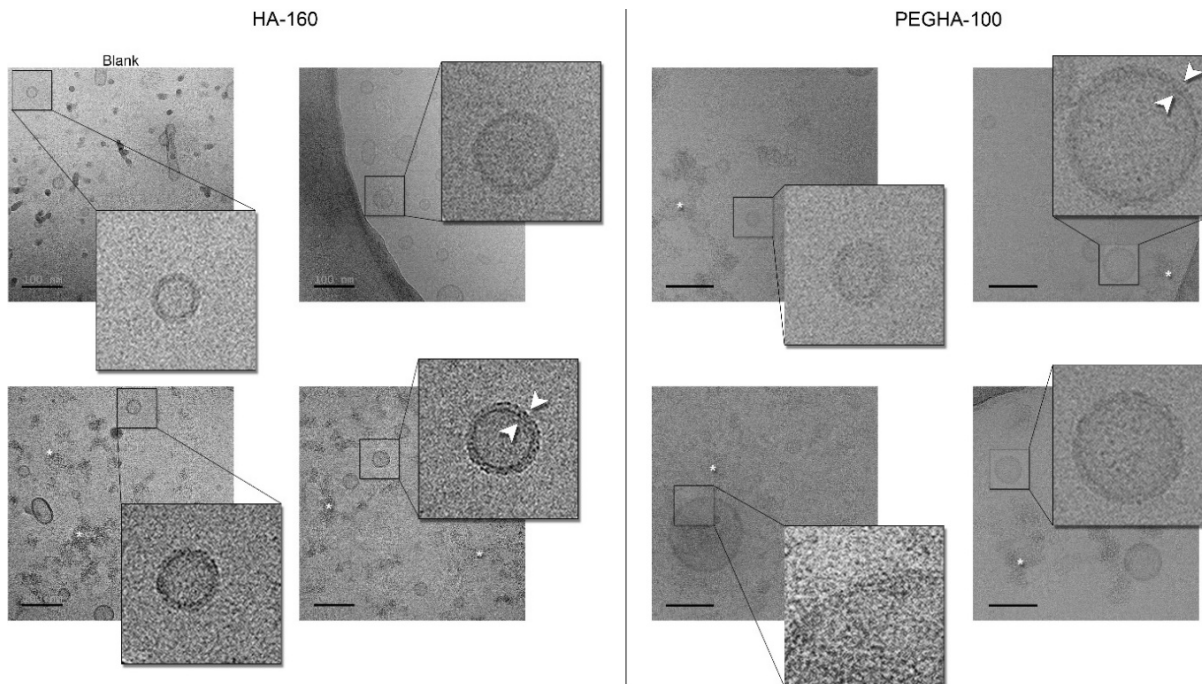


Figure 4 Morphological characterization of HANAs. A gallery of cryo-TEM micrographs with a blank HA-160, BVZ-loaded HA-160, and BVZ-loaded PEGHA-100; zoomed regions magnified 4× from the original size. The white arrows and asterisk mark the bilayer and irregular aggregates, respectively. Micrographs and zoomed areas have been optimized in brightness and contrast for visual clarity in Fiji image processing package (<https://imagej.net/software/fiji/>); high-contrast blobs in the blank HA-160 due to ethane contamination. Scale bars: 100 nm.

inferred the architecture of the HANAs, core-shell nanostructures with a hydrophilic core enclosed by a bilayer, wherein the mAb plays a pivotal role in their conformation. Importantly, it is worth highlighting that this type of polymer-lipid NPs has not been previously reported for the delivery of mAbs.

2.4 The assembling dynamics of HANAs by computational modeling

Understanding the self-assembly process of novel nanocarriers will serve as feedback to accelerate the development process of further candidates. Herein, the assembling dynamic of NPs aiming to deliver mAbs will be explored by computational modeling.

The starting systems were constructed by placing the excipients of HA-160 (Fig. 5(a)) and PEGHA-100 (Fig. 5(b)), and the mAb randomly into box systems during 100 ns in a fixed ratio for simulating the real process of assembling. Root-mean-square displacement provided evidence that the structure of HANAs was stable with less fluctuation after ~ 25 ns, which underlines the instant assembling of the HANAs. Initially, the shape and distribution of the HANAs was elucidated by investigating the radius of gyration (R_g). From the molecular level, Fig. 5(c) exhibited the smallest R_g for PEGHA-100 (~ 5.5 nm), which is translated into a smaller size than HA-160 (R_g ~ 7 nm). Moreover, the similarities found among the centroidal axes of the R_g for PEGHA-100 suggested the homogeneity, and more likely, spherical shape, in line with the observations displayed by cryo-TEM.

To elucidate the structural configuration of HANAs, we chose to study in detail the nature of the interactions utilizing hydrogen bond, hydrophobic, coulomb, and van der Waals interactions as the driving forces behind assembly (Fig. 5(d)). In general, the self-aggregation of excipients rather than with the mAb was obvious in HA-160. In contrast, we observed a strong preference of the excipients for the mAb in PEGHA-100. The aggregation phenomenon by the formation of H-bonds, a classical weak non-bonded force with a dominant role in the behavior of drug delivery systems [58, 59]. Indeed, the average number of H-bonds with BVZ had an order of HAC16 > Lipoid S100 for HA-

160 and Lipoid S100 > HAC16 > DSPE.PEG_{2k} for PEGHA-100. Furthermore, the calculated interaction energy consisting of Lennard-Jones (LJ-SR) and coulomb potential (Coul-SR) showed a stronger binding ability between mAb and excipients in PEGHA-100 (total energy: -2864.2 kJ/mol, compared to HA-160 (total energy: -1773.3 kJ/mol)) (Fig. S4 in the ESM). In addition, the solvent-accessible surface area (SASA) was used to evaluate the hydrophobic interaction of the HANAs with the mAb HANAs (Figs. 5(e) and 5(f)). In agreement with the superior lipid composition of PEGHA-100, we observed an SASA value of 33369.3 Å², which further supports the greater compactness of this candidate.

To investigate the binding specificity of BVZ-excipients further, we analyzed interaction details and contacted amino acids among existing components.

Regarding the interaction details, similar patterns were observed for both HANAs (Figs. 5(e) and 5(f)). The polar headgroup (yellow circle) and hydrophobic chain (black circle) of Lipoid S100 exhibited a remarkable binding affinity for the acid and nonpolar amino acids of BVZ, respectively. In line, the carboxylic groups of the HAC16 demonstrated higher interaction with the basic amino acids. Notably, serine (which comprises 13% of the total amino acids [60]) represented the most contacted amino acid (Fig. S5 in the ESM), followed by proline (HA-160), and threonine (PEGHA-100).

These results underline how the different composition and molar ratios influenced the interaction patterns leading to HANAs formation. Similarly, the amino acids sequence plays a pivotal role in the interaction's phenomena. This is supported by the conclusions drawn after studying the assembling dynamics by DLS and AF4 (see Fig. S6 in the ESM). Even though homogeneous populations have not been observed, the interactions of BVZ with HAC16 or Lipoid S100 were evident. These results validate our formulation rationale. The entrapment of the mAb within the nanoassemblies is initiated by triggering ionic interactions, between the negative charge of the polymer and the cationic aminoacids of the mAb molecules, and also, hydrophobic interactions of the C16 region of the polymer and

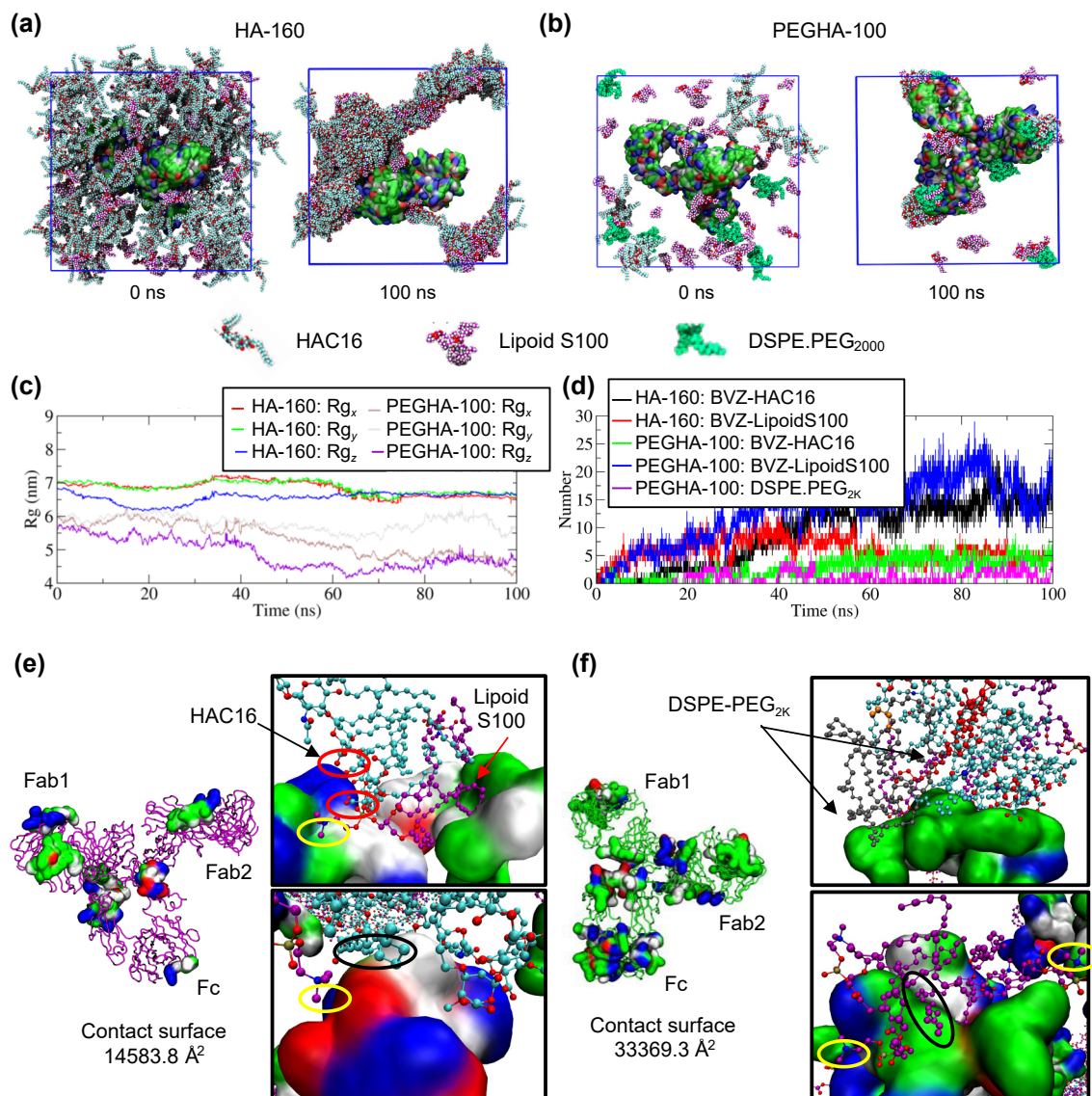


Figure 5 The assembling dynamics of BVZ-loaded HA-160 and PEGHA-100. Initial and 100 ns later configuration of one molecule of BVZ and the components of (a) HA-160 and (b) PEGHA-100 by MD simulation. (c) Radius of gyration of HA-160 and PEGHA-100, and (d) contacts characteristics based on number of hydrogen bonds (H-bonds) between antibody BVZ and excipients. SASA (left image) and interaction details (right boxes) among existing components in (e) HA-160 and (f) PEGHA-100. In SASA, the interaction residues on the mAb were emphasized with a rainbow surface. Interaction details showed the details on the structural property (each component has been arrowed; yellow, black and red circles indicate the polar head group and hydrophobic chain of Lipoids S100 and the carboxyl groups of HAC16, respectively; and the green, blue, and white surface indicated the acid, basic and nonpolar amino acid residues, respectively).

the Lipoid S100. Such interactions could occur at the level of the phospholipids/polymer with the hydrophilic regions of the mAb protruding towards the internal aqueous core or the external aqueous phase.

2.5 Association capacity of BVZ to the HANAs

Following the screening detailed in the preceding section, the HANAs underwent characterization in terms of BVZ association efficiency and corresponding loading capacities, as detailed in Table 2. The results showed that the quantities of essential constituents influenced the BVZ association efficiency (67%–99%) and loading capacity (22%–47%, w/w). These are outstanding as compared with those disclosed in previous reports [28, 31].

2.6 Stability of HANAs in simulated biological media and release profile

A critical feature of nanoparticulate drug delivery systems is their stability in plasma. Thus, the colloidal stability of selected prototypes was evaluated upon incubation in PBS-10% FBS (Fetal bovine serum) and PBS at 37 °C. A general pattern representing

an increment of the particle size followed by size reduction and stabilization was observed (Fig. 6). Given the fact that HANAs are stable in PBS, it could be induced that FBS proteins influence the observed pattern [61]. Despite the size transition observed, it could be assumed that HANAs exhibit an adequate colloidal stability for at least 8 h under bio-relevant conditions.

Although HA-200 based HANAs displayed an acceptable stability profile and a high loading capacity (LC), they were excluded from subsequent studies because of their larger size as compared to other prototypes.

Throughout this work, we have hypothesized that the strong interactions between the mAb and the HANAs would prevent the premature release of the cargo. Hence, HANAs HA-160, HA-100, and PEGHA-100 were selected to probe this hypothesis and assess whether the superior amount of HAC16 in the formulation process or the presence of PEG leads to a different release kinetics. The results presented in Fig. 7 show a less than 20% burst release for all prototypes, followed by a very slow release over the time, except for HA-100 (~ 52% after one week at pH 5.0). This specific prototype (HA-100) was made of particularly low amounts of

Table 2 Physicochemical properties, association efficiency (AE, % w/w) and loading capacity (LC, % w/w) of the HANAs.

Prototype	Physicochemical properties			AE (%)	LC (%)
	Particle size (nm)	PDI	Zeta potential (mV)		
HA-200 ^a	196 ± 13	0.24	-14 ± 1	99 ± 0.3	47 ± 0.1
HA-160 ^b	162 ± 17	0.23	-13 ± 2	86 ± 11	34 ± 4
HA-100 ^b	107 ± 14	0.23	-13 ± 3	74 ± 11	30 ± 4
PEGHA-100 ^b	79 ± 8	0.25	-13 ± 2	67 ± 21	22 ± 7

The physicochemical properties were determined by dynamic light scattering (particle size and PDI) and laser Doppler anemometry (Zeta potential). Data are expressed as mean ± SD, $n \geq 3$. NPs were developed with the HAC16 DS 10%–15%^a and DS 1%–10%^b polymers.

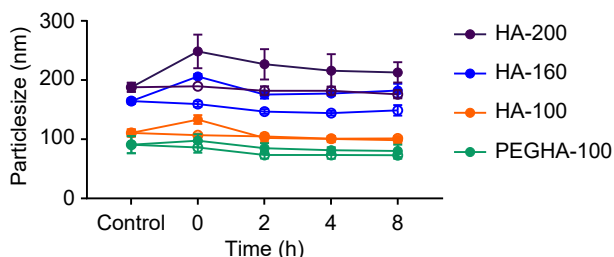


Figure 6 Stability in simulated biological fluids at 37 °C. BVZ-loaded HANAs were incubated in PBS supplemented with 10% FBS (fill dots) and PBS (empty dots), and the distributive and cumulative particle size were evaluated overtime by DLS, respectively. Control indicates the particle size of the HANAs prior incubation. Statistical comparisons were done following a parametric unpaired t-test without significant differences in terms of particle size between the control and 8 h ($P < 0.05$). Data are represented as mean ± SD, $n = 3$.

starting materials, a fact that may have led to a loose interaction among them and a different architectural organization. To further prove that the amount of released mAb retained its active conformation, the total amount of free BVZ was determined by AF4 with UV and refractive index (RI) detectors, rendering comparable values to the ones determined by enzyme-linked immunosorbent assay (ELISA) (see Fig. S7 in the ESM).

We have postulated that the slow release of BVZ over the time under the selected *in vitro* conditions may be attributed to the robust interactions among the mAb and the HANAs components. In an *in vivo* situation, it could be speculated that the mAb release might occur within intracellular compartments where high concentrations of enzymes (e.g., phospholipase and hyaluronidases) would drive the disassembling of the nanostructures [62–64]. In fact, the results obtained in the *in vitro* studies support this assumption. This specific release profile might be promising for preventing premature release in the blood circulation, often observed for biological drugs.

In brief, here we have provided a detailed description of the characterization of the HANAs technology for delivering mAbs, compiling most of the MIRIBEL recommendations for

nanotechnologies [44]. The remarkable association efficiency (67%–99%) and loading capacities (22%–47%, w/w), and the control of release, observed for very small size HANAs are especially singular (see Table S2 in the ESM). As far as we are aware, this is the first BVZ-delivery system to show these highly desirable features.

In a following step, we aimed to explore the *in vitro* performance of the most promising HANAs, HA-160 and PEGHA-100. For this purpose, HANAs were labeled with the fluorescent dye DiD without modifying their main physicochemical properties (Table S3 in the ESM).

2.7 *In vitro* cytotoxicity

To assess the toxicity profile of the HANAs, cell viability was studied in lung cancer (CMT 167) and macrophages (RAW 264.7) cell lines (Fig. 8). A reduction in the cell viability of 30% was considered to be toxic (ISO 10993-5 standards) [65]. Interestingly, HA-160 (Fig. 8(a)) and PEGHA-100 (Fig. 8(b)) HANAs prototypes exhibited a very low toxicity profile upon incubation with CMT167 cells for all concentrations tested. By contrast, a trend toward size-dependent toxicity was observed in RAW 264.7 cells. Regardless of the NPs composition, we speculate that the small reduction in cell viability observed for PEGHA-100 may be attributed to the small particle size. Although this outcome has been previously described [66], the size-dependent uptake by macrophages is controversial since early reports suggest a direct correlation between the particle size and the magnitude of the uptake [14, 67]. Irrespective of the size-dependent toxicity profile observed in macrophages, it should be noted that toxicity is only apparent when the concentration of HANAs is as high as 2 mg/mL.

2.8 Uptake and cellular internalization of the HANAs

An important objective of this work was to assess the capacity of HANAs for intracellular delivery of mAbs. This transport of the mAbs to the intracellular compartments is essential for targeting relevant intracellular oncoproteins. Consequently, cellular uptake

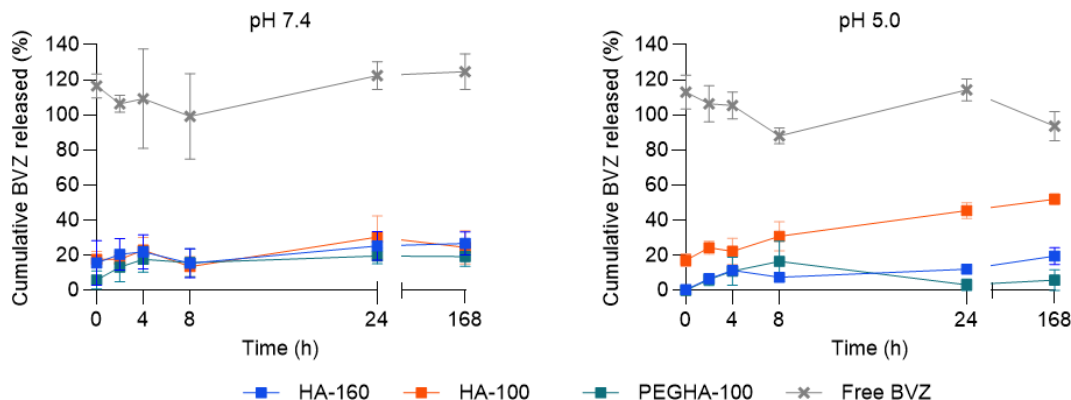


Figure 7 Release profile of HANAs upon incubation in PBS pH 7.4 and 5.0 at 37 °C. The cumulative amount of released BVZ was quantified by ELISA. As control, free BVZ was treated in the same conditions than the NPs. Data are represented as mean ± SEM, $n \geq 3$. Following an unpaired t-test between groups at pH 7.4 and pH 5.0, significant differences among HA-100 and HA-160, HA-100 and PEGHA-100 were observed at 0, 2, 24 and 168 h with pH 5.0 ($P < 0.05$).

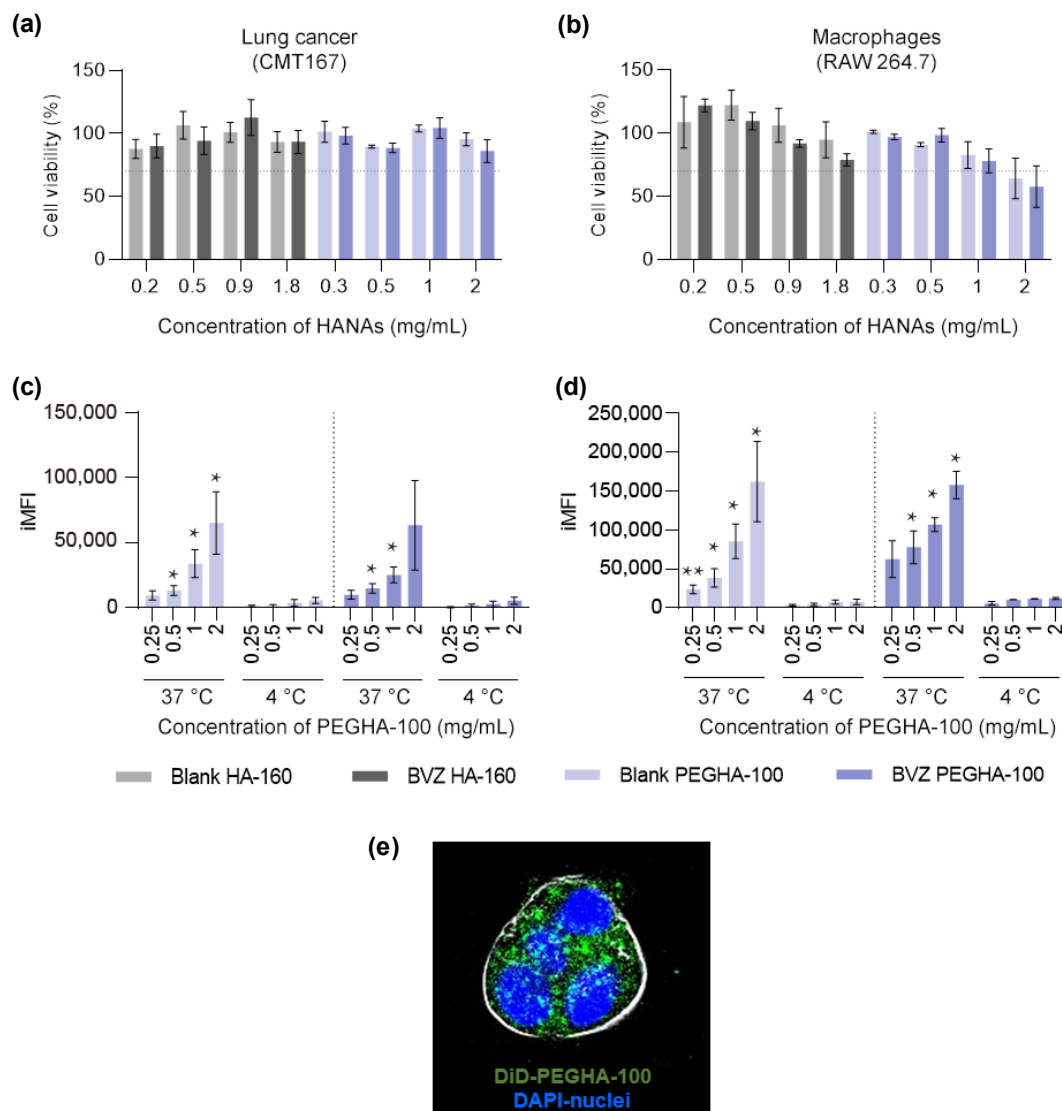


Figure 8 Metabolic activity and cellular uptake of DiD-labelled HA-160 and PEGHA-100. Cell viability in (a) CMT 167 and (b) RAW 264.7 cell lines after 24 h of exposure. Cells were exposed to increasing concentrations of blank and BVZ-loaded HANAs. Cell viability values below 70% were considered toxic (dashed lines). Cellular uptake of blank and BVZ-loaded PEGHA-100 in (c) CMT 167 and (d) RAW 264.7 following 4 h of incubation at 37 and 4 °C at increasing concentrations of HANAs. (e) Representative confocal microscopy images of blank PEGHA-100 after 24 h of incubation in the lung cancer cell line. The membrane was recorded by bright-field microscopy. Statistical comparisons were done following a parametric unpaired t-test between temperatures (* $P < 0.05$, ** $P < 0.01$). iMFI integrated mean fluorescence intensity. Data are expressed as mean \pm SEM, $n \geq 3$.

studies at 37 °C were conducted using CMT 167 lung cancer cell line and macrophages (RAW264.7) as previously described. Studies were also performed in parallel at 4 °C to elucidate a potential passive uptake mechanism [68].

The results disclosed in Figs. 8(c) and 8(d) show the lack of fluorescence at 4 °C, thus ruling out a passive transport mechanism. In contrast, at 37 °C, a significant dose-dependent transport was observed in both cell lines, this being more remarkable in macrophages, a result that is consistent with their phagocytic nature. The confocal microscopy images show defined intracellular fluorescence spots in the lung cancer cell line (Fig. 8(e)). These uptake results may be, at least partially, related to the high affinity of HA towards the CD44 receptor, overexpressed in CMT167 [69] and macrophages [70, 71], which ultimately causes receptor-mediated endocytosis [72, 73]. Overall, this study allowed us to conclude about the high efficiency of the HANAs as intracellular delivery systems.

2.9 Scaling-up and stability of HANAs technology

From an industrial perspective, the definition and characterization of quality attributes of nanomedicine candidates is crucial,

especially in the context of a large-scale production [74]. For instance, Dormont et al. have reported the physicochemical and cytotoxicity differences between lab- and industrial-scale batches during the scale-up of squalene-adenosine NPs [75]. Herein, the scaling up the HANAs from the starting batch size (1 mL) to a volume suitable for a clinical setting was performed using microfluidics and regular magnetic stirring production.

Microfluidics offers the opportunity to produce NPs in a reproducible way, with the additional advantage of scalability and particle size tuneability [76]. In this study, the flow ratio was kept constant (12.5:1, HAC16-BVZ:Lipoid S100), and the influence of the flow rate was screened from 2 to 18 mL/min. The results showed a significant decrease of HANAs particle size as the flow rate increased (Fig. S8 in the ESM), achieving monodisperse and reproducible production at the highest flow rate investigated.

As an alternative for the large-scale production of HANAs, we explored the possibility to produce large batches using a blade agitator. The volume of each phase was increased proportionally while the concentration of materials was kept. As shown in Table 3, the quality control parameters (particle size, PDI, surface charge, and association efficiency) show similar values in this 50 mL-batch as compared to the values obtaining in the small batch (1 mL).

Table 3 Physicochemical properties, AE (%), and LC (%) of the scale-up using microfluidics and bench mode compared to the small-size batch of HA-160

Prototype (batch)	Physicochemical properties			AE (%)	LC (%)
	Particle size (nm)	PDI	Zeta potential (mV)		
Small batch (1 mL)	162 ± 17	0.23	-12 ± 1	86 ± 11	34 ± 4
Microfluidics	211 ± 16	0.22	N.D.	N.D.	N.D.
50 mL-batch	157 ± 00	0.15	-15 ± 0	64 ± 00	N.D.

The physicochemical properties were determined by dynamic light scattering (particle size and PDI) and laser Doppler anemometry (Zeta potential). Data are expressed as mean ± SD, $n \geq 3$, except 50 mL-batch, $n = 1$. N.D. not determined.

In conclusion, the described methods were proven suitable for the large-scale production of HANAs. Stands out the batch-mode production due to its simplicity, superior production yields and preservation of the main physicochemical properties, features to be considered in their industrial translation.

To further assess the potential of the HANAs from a translational perspective, the long-term stability during storage was studied by analyzing the colloidal stability at 4 °C. As reflected in Fig. 9, the HANAs were stable for at least 3 months.

The long-term stability of representative freeze-dried HANAs (HA-160) (Fig. 10) was also conducted following the ICH guidelines [77]. HANAs were freeze-dried using 2.5% w/v trehalose [78], and the cakes were stored at 5 °C and 25 °C/60% relative humidity. The results showed that the quality attributes of freeze-dried HANAs in terms of particle size, PDI, and surface charge were maintained for at least one year.

In summary, in this work we have adopted a comprehensive approach to evaluate the reproducibility of the HANAs assembling process using standardized manufacturing procedures

and detailing each step from raw material sourcing to final product formulation. Batch-to-batch consistency studies were conducted using identical protocols thorough evaluation of key characteristics such as particle size, surface charge, association efficiency, and physical appearance. Accelerated stability studies assessed long-term stability under varied storage conditions, following the ICH guidelines. Periodic analysis of physical parameters ensured consistent quality and long-term stability of our HANAs technology.

3 Conclusions

Here we disclose a new composition of HAC16-based nanoassemblies (HANAs) specially adapted for the entrapment of clinical doses of mAbs. These nanostructures exhibit the requisite features to overcome biological barriers, including a targeted particle size of 100 nm, neutral surface charge, and high loading capacities. Comprehensive characterization provided evidence of the formation of core-shell nanostructures, showcasing a

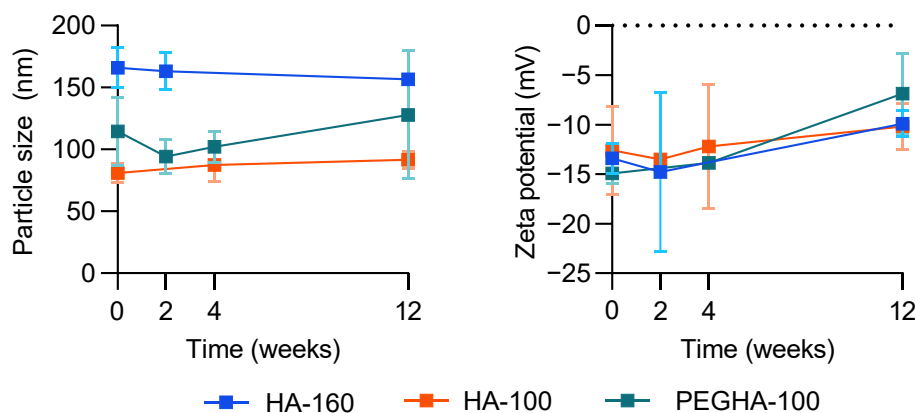


Figure 9 Stability in suspension at 4 °C. Evolution of the particle size and the surface charge of the HANAs during storage for up to 3 months. Statistical comparisons were done following a parametric unpaired or Mann-Whitney t-test without significant differences in terms of particle size or PDI ($P < 0.05$). The physicochemical properties were determined by DLS (particle size and PDI) and laser Doppler anemometry (Zeta potential). Data are expressed as mean ± SEM, $n \geq 3$.

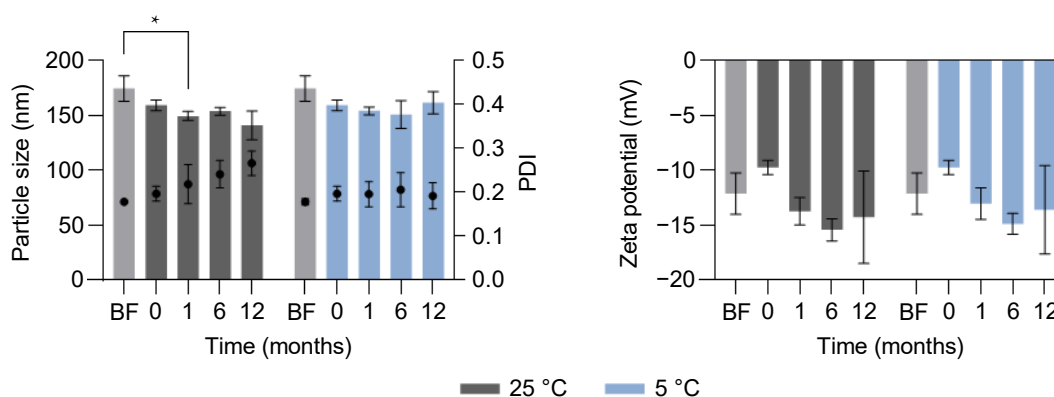


Figure 10 Stability of freeze-dried HANAs (HA-160) upon storage for 12 months at 5 and 25 °C, 60% humidity. At each time point, the freeze-dried HANAs were resuspended in water and the physicochemical properties were determined. Statistical comparisons in terms of particle size and Zeta potential were carried out by 2-way ANOVA followed by a Fisher's LSD test between the sample before freeze-drying (BF) and each time point ($*P < 0.05$). The physicochemical properties were determined by DLS (particle size and PDI) and laser Doppler anemometry (Zeta potential). Bars: particle size and Zeta potential, dots: PDI. Data are expressed as mean ± SEM, $n \geq 3$.

hydrophilic core enveloped by a bilayer. Molecular dynamic simulation shed light on the driven forces that induce the assembly of the HANAs and the parameters determining their structural organization, suggesting the BVZ insertion into the bilayer or in the hydrophilic core of the HANAs. Beyond their favorable attributes, a low toxicity profile and a favorable uptake in relevant cancer cell lines underscore the substantial potential of HANAs for facilitating the delivery of biologicals. Defining these critical features facilitated the scale-up of the HANAs, confirming their suitability for industrial translation. Consequently, HANAs could be proposed as promising nanocarriers for the extracellular and intracellular delivery of mAbs.

4 Experimental

4.1 Reagents and materials

The humanized mAb BVZ was kindly donated by mAbxience (Spain). Sodium palmitoyl hyaluronate (HAC16) of 30–70 kDa, DS 1%–10%, and DS 10%–15% were purchased from Contipro a.s. (Czech Republic). Phosphatidylcholine from soybean (Lipoid S100) and N-(carbonyl-methoxypolyethylenglycol-2000)-1,2-distearoyl-sn-glycero-3-phosphoethanolamine (DSPE.PEG_{2K}) were obtained from Lipoid GmbH (Germany). FBS was obtained from Gibco (Thermo Fisher Scientific, USA). 1,1'-Dioctadecyl-3,3,3',3'-Tetramethylindodicarbocyanine (DiD) was obtained from Invitrogen, Thermo Fisher Scientific (USA). Resazurin sodium salt, Triton X-100, and Accutase® were acquired from Sigma-Aldrich (Darmstadt, Germany). The 96 multiwells plate and recombinant Human VEGF₁₆₅ were provided by Thermo Fisher Scientific (USA). Goat anti-human IgG HRP conjugated was obtained from Jackson Immuno Research Laboratories, Inc. (USA). 2,2'-azino-di-(3-ethylbenzthiazoline sulfonic acid (ABTS) solution was acquired from Roche (Switzerland).

4.2 Preparation of the HANAs

A self-assembling method was used to prepare the HANAs. Briefly, 125 μ L of an aqueous solution of BVZ (final concentration ranging from 0.5 to 5 mg/mL) was added to 500 μ L of an HAC16 solution (final concentration ranging from 0.25 to 2 mg/mL) under magnetic stirring at 1100 rpm and room temperature. Subsequently, 50 μ L of an ethanolic solution containing different concentrations of Lipoid S100 (final concentration of 0.25, 0.5, or 1 mg/mL) was added dropwise over the above mixture. Finally, the volume was made up to 1 mL with PBS. In the case of HANAs containing the PEGylated, lipid DSPE.PEG_{2K} was added in the ethanolic phase, maintaining the final volume (25 μ L of Lipoid S100 and 25 μ L of DSPE.PEG_{2K}).

HAC16 polymers were dissolved in ethanol/ultrapure water using minimal ethanol (i.e., for HAC16 30–70kDa DS 1%–10% and DS 10%–15%, 40% v/v and 50% v/v, respectively).

Fluorescent-labeled HANAs were prepared, adding 25 or 10 μ L of DiD into the ethanolic phase. Thus, 50 μ L of this phase was added over the system to reach a DiD final concentration of 10 μ g/mL (HA-160) or 1 μ g/mL (PEGHA-100), respectively, in a final formulation volume of 1 mL.

HANAs were concentrated to a final BVZ concentration of 3.2 mg/mL by a Tangential flow filtration (TFF) system or nitrogen source. In the case of the TFF method, the HANAs were submitted to the KrosFlo® KR2i TFF system (Repligen, Waltham, MA) with 100 kDa MWCO membrane. A total of 5 diafiltrations were performed, followed by a concentration procedure using PBS as eluent at a flow rate of 12 mL/min.

4.3 Microfluidics

A NanoAssemblr® Benchtop device (Precision Nanosystems, Vancouver, Canada) was used for the preparation of HA-160.

First, HAC16 was mixed with BVZ at a flow rate of 14 mL/min at a feed ratio of 4:1. For the addition of Lipoid S100 to the HAC16/BVZ solution (produced in the bench), a feed ratio of 12.5:1 HAC16-BVZ: Lipoid S100 at increasing flow rates (from 2 to 18 mL/min) was applied.

4.4 Batch-mode scale up

Scaling-up of the primary prototypes to a 50 mL volume batch was performed in a 250 mL beaker. A volume of 6.25 mL of an aqueous solution of BVZ (2 mg/mL, final concentration) was poured over 25 mL of a hydroalcoholic solution of HAC16 30–70 kDa DS 1%–10% (2 mg/mL, final concentration) under mechanical stirring at 680 rpm (RW 20 DZM propeller stirrer, IKA Spain). Over it, dropwise, 2.5 mL of an ethanolic solution of Lipoid S100 (1 mg/mL, final concentration) was added. Then, the volume was made up to 50 mL with PBS. NPs were finally diafiltrated and concentrated up to 3.2 mg/mL BVZ by TFF as described in section 4.2. Likewise, the main physicochemical properties of the NPs were characterized by DLS (see section 4.5).

4.5 Physicochemical characterization

Particle size and PDI were measured by DLS, and the Zeta-potential was measured by laser Doppler anemometry (LDA) using a Malvern Zeta-Sizer (NanoZS, ZEN 3600, Malvern Instruments, UK). Samples were diluted in PBS, accordingly. A cumulant analysis obtained the hydrodynamic diameter calculated as the Z-average value based on intensity distribution.

NTA (NanoSight NS3000, UK) was performed after diluting 1:1000 or 1:10000 in PBS and recorded at 25 °C. Measurements consisted of 5 videos for 60 s each and proceeded with the NTA software v3.3.

4.6 Morphological characterization by cryo-TEM

Cryo-TEM was conducted to evaluate the morphology and structure of the HANAs designated as HA-160 and PEGHA-100. Prior to 2D imaging, a 3 μ L volume of the HA-160 sample was applied onto a Cu 300-mesh Quantifoil® R2/2 grid. The sample was then incubated for 30 s before being vitrified using an EM GP2 automatic plunge freezer (Leica). Vitrification was achieved with a 1.5-s blot-time, carried out in conditions of over 90% humidity and approximately 8 °C. Data acquisition was carried out on a JEM-2200FS/CR (JEOL, Ltd.) 200 kV TEM equipped with a K2 Summit direct detection camera (GATAN) at 25,000 \times or 30,000 \times for high magnification imaging. The PEGHA-100 sample was vitrified using a Vitrobot Mark IV plunge freezer (Thermo Fisher Scientific), applying 4 μ L of diluted sample (2 units of PEGHA-100 per 1 unit of PBS) onto a Cu 300-mesh Quantifoil® R2/1 grid with 20 s of incubation. The vitrification process involved a 3-s blot-time with the application of a -2-offset value. This was carried out under conditions of 70%–80% humidity and at room temperature. 2D cryo-imaging of PEGHA-100 was performed as for the HA-160 sample.

4.7 AF4

AF4 measurements were performed using an AF2000 separation system (Postnova Analytics, Landsberg, Germany) equipped with PN1130 isocratic pumps and degasser, an inline polyvinylidene fluoride (PVDF) filter 0.1 μ m (Millipore, MA, USA) and an autosampler with an injection loop of 103 μ L. The separation was performed on a channel utilizing a regenerated cellulose (RC) membrane with 1 kDa MWCO and a Teflon spacer with a thickness of 350 μ m. For the release studies, the area of the refractive index (RI) and UV (280 nm) signals were used to determine the percentage of free mAb after the injection of the corresponding amount of free BVZ, used as a control. The AF4

equipment was coupled online with a UV–vis spectrophotometer (PN3211), a multi-angle laser light scattering (MALS, PN3609), and a refractive index detector (RI, PN3150).

4.8 SAXS

SAXS measurements were performed in the BL11 NCD-SWEET beamline from the ALBA Synchrotron Light source in Barcelona, Spain. Samples were placed in a Kapton windows sample holder suitable for liquids. The incoming beam energy was set at 15 and 8 keV with a sample detector distance of 3600 mm. 2D patterns were recorded in a Pilatus 1M (Dectris, Switzerland) detector. Ninety patterns per sample were recorded during 1 s of exposure time, where no radiation damage effects were observed during measurements. Isotropic 2D patterns were integrated using the pyFAI library. Vesicles were modeled with a multi-shell spherical model to consider the bilayer shell.

4.9 In silico modeling of HANAs

To study the binding mechanism of the Ab with the components of the system, a molecular dynamic (MD) simulation was conducted. The simulated systems of BVZ-loaded HA-160 and PEGHA-100 were manually set up. AMBER14SB and GAFF all-atom force-field were used to describe the motion process of BVZ-loaded HANAs based on the Gromacs2020 package and accelerated by GPU NVIDIA GeForce RTX 3090 and CPU Intel (R) Core (TM) i7-10700F @ 2.90GHz [79, 80]. The bond length, angle, and dihedral value for HAC16, DSPE.PEG₂₀₀₀ and Lipid S100 were generated using Sobtop [81], and the restrained electrostatic potential charges of the lipids were computed by Gaussian at B3LYP(D3)/6-311G** level [82, 83] and calculated with Multiwfn [84]. The MMFF94 charges were given to HAC16 using Openbabel [85]. All molecules were put into the vacuum box 1 nm away from the box border and solvated the box with the TIP3P water model. The counter ions were added into the solvated box to keep an electroneutral system.

After constructing the initial model, energy minimization was executed with the steepest descent method to keep the maximum force lower than 1000.0 kJ/mol/nm and eliminate the irrational contacts in the systems. A total time of 500 picoseconds (ps) of an isothermal isobaric simulation was carried out to pre-equilibrate the systems. Afterward, 100 nanoseconds (ns) MD production was performed and coupled isotropically with a 4.5×10^{-5} compressibility and coupling constant of 12.0 ps under the Parrinello–Rahman algorithm [86]. The temperature was set at 298.15 K and paired with a coupling constant of 1.0 ps under the v-rescale algorithm [87]. The cutoff distance of short-range van der Waals and electrostatic interactions was set at 1.0 nm, and the Particle Mesh Ewald algorithm was employed to compute the long-range electrostatic interaction [88]. In the whole process, the integral of dynamics was calculated every 2 femtoseconds (fs), and the relevant trajectories were written every 10 ps. Visual Molecular Dynamics [89] and Qtgrace [90] were hired to visualize the motion trajectory, H-bond property, and conformation change.

The dynamics assembling of the HANAs was constructed in an $18 \times 18 \times 18$ nm³ box. The total atom number of HA-160 and PEGHA-100 was 604,487 and 604,797, respectively, calculated based on the theoretical composition in mg/mL and the MW of each material.

The radius of gyration was calculated by using the below equation (Eq. (1)), in which m_i for atom i quality, r_i for atom i mass center position relative to the molecule.

$$R_{g,x} = \left(\frac{\sum_i (r_{i,y}^2 + r_{i,z}^2) m_i}{\sum_i m_i} \right)^{\frac{1}{2}} \quad (1)$$

The SASA was calculated to measure the contact area with excipients, and the sphere's radius to probe the molecule's area was set as 1.4 Å.

4.10 Association efficiency and loading capacity

BVZ association efficiency to HANAs was quantified using an ELISA. NPs were isolated by ultracentrifugation (35,000 rpm, 1.5 h, 15 °C) using a Beckman Coulter (optime L90K) ultracentrifuge equipped with a Beckman type 70.1 Ti rotor. The amount of free BVZ in the supernatant was recovered and quantified. As a control, a solution of BVZ at 3.2 mg/mL was treated in the same conditions and subsequently quantified.

A 96-multiwell plate was coated with 0.005 µg antigen/well (i.e., recombinant human VEGF165) at a concentration of 0.05 µg/mL (100 µL/well) and incubated overnight at 4 °C. The antigen was prepared in a coating buffer (1.59 mg/mL, Na₂CO₃, 2.94 mg/mL, NaHCO₃, pH 9.6). After the antigen attachment, the plate was washed four times with washing buffer (Tween 20 0.05% (v/v) in PBS, pH 7.4). The process was followed with a blocking step that was performed with 300 µL/well of blocking buffer (2% v/w of dry milk powder prepared in washing buffer) for 2 h at 37 °C under orbital shaking at 300 rpm. By the end, another washing step is done, and the antigen-coated plate is ready to use. Calibration curves were done by diluting accordingly and loading the samples on the previously prepared antigen-coated plate (incubation for 1 h at 37 °C). Then, the plate was submitted to a washing step with the addition of the secondary goat anti-human HRP Ab at a concentration of 0.08 µg/mL and incubated for 1 h at 37 °C. Finally, after the last washing step, the detection substrate (ABTS) was added (50 µL/well). After 25 min of incubation at RT, sample absorbances were measured at 405 nm using a microplate reader (Synergy H4, BioTek, VT, USA). The percentage of entrapped Ab and the loading capacity of the NPs were calculated by using equations Eqs. (2) and (3), respectively, as follows:

$$AE (\%) = \frac{\text{Theoretical amount of BVZ} - \text{Free BVZ}}{\text{Theoretical amount of BVZ}} \times 100 \quad (2)$$

$$LC (\%) = \frac{\text{Associated BVZ}}{\text{Total theoretical concentration of the system}} \times 100 \quad (3)$$

4.11 Colloidal stability

The short-term colloidal stability of the HANAs in simulated biological medium was performed in PBS supplemented with 10% FBS. For this purpose, NPs were diluted 10-times in the medium and incubated at 37 °C under orbital shaking at 300 rpm. At different time points (0, 2, 4, and 8 h), particle size and PDI were evaluated by DLS. A distributive analysis was used to obtain the hydrodynamic diameter in PBS-10% FBS, calculated as the Z-average value based on intensity distribution peak by peak. As a control, NPs were diluted in PBS under the same conditions, and the cumulative analysis was reported.

The stability during storage in suspension and freeze-drying studies have been performed. The HANAs were stored in liquid form at 4 °C for suspension stability and characterized based on particle size, PDI, and Zeta potential. For the freeze-drying studies, 2.5 (w/v) of trehalose was added, then frozen at –80 °C and freeze-dried (Genesis™ 25 EL, S.P Industries, PA, USA). Then, formulations were resuspended to their original volume in ultrapure water, and their physicochemical properties and association efficiency were measured as previously described.

4.12 Release profile

The amount of active released BVZ was quantified by ELISA.

Samples were diluted 10-times in PBS at pH 7.4 and 5.0 (adjusted with 1 M NaOH solution) and incubated under orbital agitation at 37 °C. At different time points (0, 2, 4, 8, 24, 168 h), 500 μ L of the samples were isolated by ultracentrifugation (35,000 rpm, 1.5 h, 15 °C) and the free BVZ in the supernatant was analyzed. As a control, a standard of free BVZ was treated in the same conditions and quantified. The release pattern was expressed as the percentage (%) of cumulative BVZ released, calculated as follows (Eq. (4)):

$$\text{Cumulative BVZ released (\%)} = \frac{\text{Free BVZ at } t_1 - \text{Free BVZ at } t_0}{\text{Free BVZ at } t_1} \times 100 \quad (4)$$

t_0 indicates the condition before incubation, and t_1 corresponds to the condition at the time point under study.

AF4 measurements determined the total amount of free BVZ. As before, HANAs were diluted 10-times in PBS at pH 7.4 and 5.0 (adjusted with NaOH) and incubated under orbital agitation at 37 °C. 103 μ L of the non-isolated HANAs were injected into the equipment at 0, 2, 4, 8, 24, and 168 h. Online quantification of free BVZ in the formulation was feasible, either by RI or UV-vis detection. For extrapolation, standards of increasing concentrations of BVZ were treated in the same conditions and quantified.

4.13 Cell culture

CMT167 and RAW 264.7 murine-derived lung cancer and macrophage cell lines from the American Type Culture Collection (ATCC) were kindly provided by Prof. Paola Allavena, (Clinical and Research Institute Humanitas, Milan, Italy). Cells were cultured in Dulbecco's modified Eagle's medium (DMEM), supplemented with 10% FBS and 1 \times P/S (100 IU/mL Penicillin and 100 μ g/mL of Streptomycin sulfate) (Gibco (Thermo Fisher Scientific), Waltham, MA, USA) referred as culture medium and were routinely tested for mycoplasma infection.

4.14 Cell viability

CMT167 and RAW 264.7 murine-derived lung cancer and macrophage cell lines were seeded in a 96-well plate at densities of 2 \times 10³ and 5 \times 10³, respectively, in DMEM supplemented with 10% FBS, penicillin, and streptomycin for 24 h at 37 °C. Cells were incubated with increasing concentrations of BVZ-loaded and blank NPs. After 24 h of treatment, cells were treated with 100 μ L/well of Resazurin 1 \times for 40 min at 37 °C. Fluorescence intensity was measured in a plate reader (Synergy H4, BioTek, VT, USA), setting the λ_{abs} at 544 nm and the λ_{em} at 590 nm. Non-treated cells were used as positive control and considered 100% of cell viability, and cells treated with Triton X-100 0.5% (v/v) were considered negative control. Cell viability was calculated according to Eq. (5).

$$\text{Cell viability (\%)} = \frac{\text{Sample fluorescence} - \text{Negative control fluorescence}}{\text{Positive control fluorescence}} \times 100 \quad (5)$$

4.15 Uptake studies

Cells were seeded in a 24-well plate at densities of 25 \times 10³ CMT 167 and 50 \times 10³ RAW 264.7 cells/well. Cells were treated with total concentrations of BVZ-loaded NPs at 0.38, 0.75, 1.5, 3 mg/mL and the correspondent dose of blank NPs (i.e., at 3 mg/mL of HA-160, 1.8 mg/mL corresponds to the concentration of NPs and 0.8 mg/mL of mAb) and incubated either at 37 or 4 °C. On-treated cells were considered the negative control. After 4 h, the cell supernatant was discarded, and cells

were washed with cold PBS three times. Then, cells were detached from the wells with accutase for 15 min at 37 °C and collected in FACS tubes. Thereafter, cells suspensions were washed with 3 mL of cold FACS washing buffer (PBS-2% FBS) and centrifuged at 1000 rpm for 5 min. Finally, cells were fixed with 100 μ L of paraformaldehyde (PFA 4%) for 30 min. Treated cells were analyzed by flow cytometry in an FACScalibur instrument, and the resulting data were analyzed using the FlowJo software BDLifeScience. Data were represented based on integrated mean fluorescence intensity (iMFI), calculated using Eq. (6).

$$\text{iMFI} = \text{Mean fluorescence intensity} \times \text{Percentage of DiD positive cells (\%)} \quad (6)$$

To visualize the internalization capacity of the HANAs by confocal microscopy, 2 \times 10³ CMT 167 cells were plated in Millicell EZ slides (Millipore) and incubated for 24 h. After incubation, cells were exposed to blank PEGHA-100 at 2 mg/mL for 24 h. Then, cells were rinsed with cold PBS 3 times and fixed in PFA 4%. Finally, coverslips were mounted in Fluoroshield™ media containing DAPI (4',6-Diamidino-2'-phenylindole) (Sigma-Aldrich). The slides were imaged in the Confocal TCS SPc5 X instrument and analyzed with the LASX software (Leica).

4.16 Statistical analysis

Data analysis was performed by using the GraphPad Prism version 9.3.0. Differences were considered significant for * P < 0.05, ** P < 0.01, *** P < 0.001 and **** P < 0.0001 with a confidence level 0.05.

ACKNOWLEDGMENTS

This work was supported by the government of Xunta de Galicia (Competitive Reference Groups, Consellería de Educación e Ordenación Universitaria, Xunta de Galicia, No. ED431C 2021/17) and by the ISCIII thorough AES 2020, Award No. AC20/00028 and within the framework of EuroNanoMed III. This work is part of the project Proof of Concept (No. PDC2021-120929-I00), financed by the Spanish Ministry of Science and Innovation-AEI/10.13039/501100011033 and the European Union NextGenerationEU/PRTR. Ana María López Estévez acknowledges a predoctoral FPU grant from the Spanish Ministry of Science, Innovation and Universities (No. FPU18/00095). Figures have been created with BioRender.com.

Electronic Supplementary Material: Supplementary material (Figure S1 Screening of different concentrations of HAC16 30–70 kDa and Lipoid S100. HAC16 polymer with two amounts of hydrophilic chains per polymer. Figure S2 Physicochemical properties of resulting prototypes. Screening of different concentrations of DSPE.PEG_{2K} over prototype HA-100. Figure S3 Cryo-TEM histogram based on diameter size of PEGHA-100. Figure S4 Interaction energy between the antibody and the remaining molecules during 100 ns MD simulation. Figure S5 Contacted amino residues among existing components in HA-160 and PEGHA-100. Figure S6 Interaction profile of the components of the HA-160 and the BVZ. Figure S7 Release profile of HA-160 upon incubation in PBS pH 7.4 and 5.0 at 37 °C by ELISA and AF4 with UV and RI detectors. Figure S8 Physicochemical characteristics of HA-160 when prepared by microfluidics technique at different flow rates and compared with the standard pipette injection (C_i). Table S1 DLS mean particle size and NTA distribution parameters of BVZ-loaded HANAs. Table S2 Summary of the most relevant nanocarriers for the entrapment of bevacizumab in cancer therapy, including the HANAs technology. Table S3 Physicochemical properties of DiD-labeled blank and

BVZ-loaded prototypes HA-160 and PEGHA-100) is available in the online version of this article at <https://doi.org/10.1007/s12274-024-6826-8>.

Open Access This article is licensed under a Creative Commons Attribution 4.0 International License, which permits use, sharing, adaptation, distribution and reproduction in any medium or format, as long as you give appropriate credit to the original author(s) and the source, provide a link to the Creative Commons licence, and indicate if changes were made.

The images or other third party material in this article are included in the article's Creative Commons licence, unless indicated otherwise in a credit line to the material. If material is not included in the article's Creative Commons licence and your intended use is not permitted by statutory regulation or exceeds the permitted use, you will need to obtain permission directly from the copyright holder.

To view a copy of this licence, visit <http://creativecommons.org/licenses/by/4.0/>.

Funding Note Open Access funding provided thanks to the CRUE-CSIC agreement with Springer Nature.

References

- Crescioli, S.; Kaplon, H.; Chenoweth, A.; Wang, L.; Visweswarajah, J.; Reichert, J. M. Antibodies to watch in 2024. *mAbs* **2024**, *16*, 2297450.
- Cruz, E.; Kayser, V. Monoclonal antibody therapy of solid tumors: Clinical limitations and novel strategies to enhance treatment efficacy. *Biologics* **2019**, *13*, 33–51.
- Mosch, R.; Guchelaar, H. J. Immunogenicity of monoclonal antibodies and the potential use of HLA haplotypes to predict vulnerable patients. *Front. Immunol.* **2022**, *13*, 885672.
- Carter, P. J.; Lazar, G. A. Next generation antibody drugs: Pursuit of the 'high-hanging fruit'. *Nat. Rev. Drug Discov.* **2018**, *17*, 197–223.
- Estévez, A. M.; Lapuhs, P.; Pineiro-Alonso, L.; Alonso, M. J. Personalized cancer nanomedicine: Overcoming biological barriers for intracellular delivery of biopharmaceuticals. *Adv. Mater.* **2024**, *36*, 2309355.
- Durán-Lobato, M.; López-Estévez, A. M.; Cordeiro, A. S.; Dacoba, T. G.; Crecente-Campo, J.; Torres, D.; Alonso, M. J. Nanotechnologies for the delivery of biologicals: Historical perspective and current landscape. *Adv. Drug Deliv. Rev.* **2021**, *176*, 113899.
- Anselmo, A. C.; Gokarn, Y.; Mitragotri, S. Non-invasive delivery strategies for biologics. *Nat. Rev. Drug Discov.* **2019**, *18*, 19–40.
- Shi, J. J.; Kantoff, P. W.; Wooster, R.; Farokhzad, O. C. Cancer nanomedicine: Progress, challenges and opportunities. *Nat. Rev. Cancer* **2017**, *17*, 20–37.
- Yu, M.; Wu, J.; Shi, J. J.; Farokhzad, O. C. Nanotechnology for protein delivery: Overview and perspectives. *J. Control. Release* **2016**, *240*, 24–37.
- Perrault, S. D.; Walkey, C.; Jennings, T.; Fischer, H. C.; Chan, W. C. W. Mediating tumor targeting efficiency of nanoparticles through design. *Nano Lett.* **2009**, *9*, 1909–1915.
- Schädlich, A.; Caysa, H.; Mueller, T.; Tenambergen, F.; Rose, C.; Göpferich, A.; Kuntsche, J.; Mäder, K. Tumor accumulation of NIR fluorescent PEG-PLA nanoparticles: Impact of particle size and human xenograft tumor model. *ACS Nano* **2011**, *5*, 8710–8720.
- Sykes, E. A.; Chen, J.; Zheng, G.; Chan, W. C. W. Investigating the impact of nanoparticle size on active and passive tumor targeting efficiency. *ACS Nano* **2014**, *8*, 5696–5706.
- Alexis, F.; Pridgen, E.; Molnar, L. K.; Farokhzad, O. C. Factors affecting the clearance and biodistribution of polymeric nanoparticles. *Mol. Pharm.* **2008**, *5*, 505–515.
- He, C. B.; Hu, Y. P.; Yin, L. C.; Tang, C.; Yin, C. H. Effects of particle size and surface charge on cellular uptake and biodistribution of polymeric nanoparticles. *Biomaterials* **2010**, *31*, 3657–3666.
- Bewersdorff, T.; Gruber, A.; Eravci, M.; Dumbani, M.; Klinger, D.; Haase, A. Amphiphilic nanogels: Influence of surface hydrophobicity on protein corona, biocompatibility and cellular uptake. *Int. J. Nanomedicine* **2019**, *14*, 7861–7878.
- Harris, J. M.; Chess, R. B. Effect of pegylation on pharmaceuticals. *Nat. Rev. Drug Discov.* **2003**, *2*, 214–221.
- Shi, L. W.; Zhang, J. Q.; Zhao, M.; Tang, S. K.; Cheng, X.; Zhang, W. Y.; Li, W. H.; Liu, X. Y.; Peng, H. S.; Wang, Q. Effects of polyethylene glycol on the surface of nanoparticles for targeted drug delivery. *Nanoscale* **2021**, *13*, 10748–10764.
- Corbo, C.; Molinaro, R.; Tabatabaei, M.; Farokhzad, O. C.; Mahmoudi, M. Personalized protein corona on nanoparticles and its clinical implications. *Biomater. Sci.* **2017**, *5*, 378–387.
- Anselmo, A. C.; Mitragotri, S. Nanoparticles in the clinic: An update. *Bioeng. Transl. Med.* **2019**, *4*, e10143.
- Tangutoori, S.; Spring, B. Q.; Mai, Z.; Palanisami, A.; Mensah, L. B.; Hasan, T. Simultaneous delivery of cytotoxic and biologic therapeutics using nanophotoactivatable liposomes enhances treatment efficacy in a mouse model of pancreatic cancer. *Nanomedicine* **2016**, *12*, 223–234.
- Deng, H. Z.; Song, K.; Zhao, X. F.; Li, Y. N.; Wang, F.; Zhang, J. H.; Dong, A. J.; Qin, Z. H. Tumor microenvironment activated membrane fusogenic liposome with speedy antibody and doxorubicin delivery for synergistic treatment of metastatic tumors. *ACS Appl. Mater. Interfaces* **2017**, *9*, 9315–9326.
- Wang, S. J.; Hüttmann, G.; Zhang, Z. X.; Vogel, A.; Birngruber, R.; Tangutoori, S.; Hasan, T.; Rahmanzadeh, R. Light-controlled delivery of monoclonal antibodies for targeted photoinactivation of Ki-67. *Mol. Pharm.* **2015**, *12*, 3272–3281.
- Tang, Y.; Soroush, F.; Tong, Z. H.; Kiani, M. F.; Wang, B. Targeted multidrug delivery system to overcome chemoresistance in breast cancer. *Int. J. Nanomedicine* **2017**, *12*, 671–681.
- Chen, P. W.; Yang, W. Q.; Hong, T.; Miyazaki, T.; Dirisala, A.; Kataoka, K.; Cabral, H. Nanocarriers escaping from hyperacidified endo/lysosomes in cancer cells allow tumor-targeted intracellular delivery of antibodies to therapeutically inhibit c-MYC. *Biomaterials* **2022**, *288*, 121748.
- Rafael, D.; Montero, S.; Carcavilla, P.; Andrade, F.; German-Cortés, J.; Diaz-Riscos, Z. V.; Seras-Franzoso, J.; Llaguno, M.; Fernández, B.; Pereira, A. et al. Intracellular delivery of anti-Kirsten rat sarcoma antibodies mediated by polymeric micelles exerts strong *in vitro* and *in vivo* anti-tumorigenic activity in Kirsten rat sarcoma-mutated cancers. *ACS Appl. Mater. Interfaces* **2023**, *15*, 10398–10413.
- Srinivasan, A. R.; Lakshmiikuttyamma, A.; Shoyele, S. A. Investigation of the stability and cellular uptake of self-associated monoclonal antibody (MAb) nanoparticles by non-small lung cancer cells. *Mol. Pharm.* **2013**, *10*, 3275–3284.
- Jiang, G. Y.; Huang, Z. L.; Yuan, Y.; Tao, K.; Feng, W. L. Intracellular delivery of anti-BCR/ABL antibody by PLGA nanoparticles suppresses the oncogenesis of chronic myeloid leukemia cells. *J. Hematol. Oncol.* **2021**, *14*, 139.
- Baião, A.; Sousa, F.; Oliveira, A. V.; Oliveira, C.; Sarmento, B. Effective intracellular delivery of bevacizumab via PEGylated polymeric nanoparticles targeting the CD44v6 receptor in colon cancer cells. *Biomater. Sci.* **2020**, *8*, 3720–3729.
- Sousa, F.; Dhaliwal, H. K.; Gattaceca, F.; Sarmento, B.; Amiji, M. M. Enhanced anti-angiogenic effects of bevacizumab in glioblastoma treatment upon intranasal administration in polymeric nanoparticles. *J. Control. Release* **2019**, *309*, 37–47.
- Abbadessa, A.; Nuñez Bernal, P.; Buttitta, G.; Ronca, A.; D'Amora, U.; Zihlmann, C.; Stiefel, N.; Ambrosio, L.; Malda, J.; Levato, R. et al. Biofunctionalization of 3D printed collagen with bevacizumab-loaded microparticles targeting pathological angiogenesis. *J. Control. Release* **2023**, *360*, 747–758.
- Pang, J. T.; Xing, H. X.; Sun, Y. G.; Feng, S.; Wang, S. Z. Non-small cell lung cancer combination therapy: Hyaluronic acid modified, epidermal growth factor receptor targeted, pH sensitive lipid-polymer hybrid nanoparticles for the delivery of erlotinib plus bevacizumab. *Biomed. Pharmacother.* **2020**, *125*, 109861.

- [32] Date, T.; Nimbalkar, V.; Kamat, J.; Mittal, A.; Mahato, R. I.; Chitkara, D. Lipid-polymer hybrid nanocarriers for delivering cancer therapeutics. *J. Control. Release* **2018**, *271*, 60–73.
- [33] Jia, Y. F.; Chen, S. W.; Wang, C. Y.; Sun, T.; Yang, L. Q. Hyaluronic acid-based nano drug delivery systems for breast cancer treatment: Recent advances. *Front. Bioeng. Biotechnol.* **2022**, *10*, 990145.
- [34] Hurt, E. M.; Kawasaki, B. T.; Klarmann, G. J.; Thomas, S. B.; Farrar, W. L. CD44/CD24^{low} prostate cells are early cancer progenitor/stem cells that provide a model for patients with poor prognosis. *Br. J. Cancer* **2008**, *98*, 756–765.
- [35] Idowu, M. O.; Kmiecik, M.; Dumur, C.; Burton, R. S.; Grimes, M. M.; Powers, C. N.; Manjili, M. H. CD44/CD24^{low} cancer stem/progenitor cells are more abundant in triple-negative invasive breast carcinoma phenotype and are associated with poor outcome. *Hum. Pathol.* **2012**, *43*, 364–373.
- [36] Payne, W. M.; Svehkarev, D.; Kyrychenko, A.; Mohs, A. M. The role of hydrophobic modification on hyaluronic acid dynamics and self-assembly. *Carbohydr. Polym.* **2018**, *182*, 132–141.
- [37] Kelkar, S. S.; Hill, T. K.; Marini, F. C.; Mohs, A. M. Near infrared fluorescent nanoparticles based on hyaluronic acid: Self-assembly, optical properties, and cell interaction. *Acta Biomater.* **2016**, *36*, 112–121.
- [38] Choi, K. Y.; Chung, H.; Min, K. H.; Yoon, H. Y.; Kim, K.; Park, J. H.; Kwon, I. C.; Jeong, S. Y. Self-assembled hyaluronic acid nanoparticles for active tumor targeting. *Biomaterials* **2010**, *31*, 106–114.
- [39] Deng, C. F.; Xu, X. H.; Tashi, D.; Wu, Y. M.; Su, B. Y.; Zhang, Q. Co-administration of biocompatible self-assembled polylactic acid-hyaluronic acid block copolymer nanoparticles with tumor-penetrating peptide-iRGD for metastatic breast cancer therapy. *J. Mater. Chem. B* **2018**, *6*, 3163–3180.
- [40] Le, N. T. T.; Cao, V. D.; Nguyen, T. N. Q.; Le, T. T. H.; Tran, T. T.; Thi, T. T. H. Soy lecithin-derived liposomal delivery systems: Surface modification and current applications. *Int. J. Mol. Sci.* **2019**, *20*, 4706.
- [41] Sharifi, S.; Mahmoud, N. N.; Voke, E.; Landry, M. P.; Mahmoudi, M. Importance of standardizing analytical characterization methodology for improved reliability of the nanomedicine literature. *Nanomicro Lett.* **2022**, *14*, 172.
- [42] Leong, H. S.; Butler, K. S.; Brinker, C. J.; Azzawi, M.; Conlan, S.; Dufès, C.; Owen, A.; Rannard, S.; Scott, C.; Chen, C. Y. et al. On the issue of transparency and reproducibility in nanomedicine. *Nat. Nanotechnol.* **2019**, *14*, 629–635.
- [43] National Institutes of Health. *Nanotechnology Characterization Laboratory (NCL)* [Online]. <https://www.cancer.gov/nano/research/ncl>.
- [44] Faria, M.; Björnmalm, M.; Thurecht, K. J.; Kent, S. J.; Parton, R. G.; Kavallaris, M.; Johnston, A. P. R.; Gooding, J. J.; Corrie, S. R.; Boyd, B. J. et al. Minimum information reporting in bio-nano experimental literature. *Nat. Nanotechnol.* **2018**, *13*, 777–785.
- [45] Publications Office of the European Union. *Guidance on the Determination of Potential Health Effects of Nanomaterials Used in Medical Devices* [Online]. 6 January 2015. <https://op.europa.eu/en/publication-detail/-/publication/e9899821-e4d4-4ceb-aada-0c62ce6cfcd3>.
- [46] Courtois, F.; Agrawal, N. J.; Lauer, T. M.; Trout, B. L. Rational design of therapeutic mAbs against aggregation through protein engineering and incorporation of glycosylation motifs applied to bevacizumab. *mAbs* **2016**, *8*, 99–112.
- [47] Goyon, A.; Excoffier, M.; Janin-Bussat, M. C.; Bobaly, B.; Fekete, S.; Guillarme, D.; Beck, A. Determination of isoelectric points and relative charge variants of 23 therapeutic monoclonal antibodies. *J. Chromatogr. B* **2017**, *1065–1066*, 119–128.
- [48] Filipe, V.; Hawe, A.; Jiskoot, W. Critical evaluation of nanoparticle tracking analysis (NTA) by nanosight for the measurement of nanoparticles and protein aggregates. *Pharm. Res.* **2010**, *27*, 796–810.
- [49] Brewer, A. K.; Striegel, A. M. Particle size characterization by quadruple-detector hydrodynamic chromatography. *Anal. Bioanal. Chem.* **2009**, *393*, 295–302.
- [50] Malvern. Zetasizer Nano User Manual. MAN0485. January 2013.
- [51] Pedersen, J. S. Analysis of small-angle scattering data from colloids and polymer solutions: Modeling and least-squares fitting. *Adv. Colloid Interface Sci.* **1997**, *70*, 171–210.
- [52] Hammouda, B. A new Guinier-Porod model. *J. Appl. Crystallogr.* **2010**, *43*, 716–719.
- [53] Paula, S.; Volkov, A. G.; Van Hoek, A. N.; Haines, T. H.; Deamer, D. W. Permeation of protons, potassium ions, and small polar molecules through phospholipid bilayers as a function of membrane thickness. *Biophys. J.* **1996**, *70*, 339–348.
- [54] Kenworthy, A. K.; Hristova, K.; Needham, D.; McIntosh, T. J. Range and magnitude of the steric pressure between bilayers containing phospholipids with covalently attached poly(ethylene glycol). *Biophys. J.* **1995**, *68*, 1921–1936.
- [55] Liu, L. Y.; Zhou, C. P.; Xia, X. J.; Liu, Y. L. Self-assembled lecithin/chitosan nanoparticles for oral insulin delivery: Preparation and functional evaluation. *Int. J. Nanomedicine* **2016**, *11*, 761–769.
- [56] Gerelli, Y.; Di Bari, M. T.; Deriu, A.; Cantù, L.; Colombo, P.; Como, C.; Motta, S.; Sonvico, F.; May, R. Structure and organization of phospholipid/polysaccharide nanoparticles. *J. Phys. Condens. Matter* **2008**, *20*, 104211.
- [57] FDA. *Drug Products, Including Biological Products, that Contain Nanomaterials - Guidance for Industry* [Online]. 2022. <https://www.fda.gov/regulatory-information/search-fda-guidance-documents/drug-products-including-biological-products-contain-nanomaterials-guidance-industry>.
- [58] Mahdavi, M.; Rahmani, F.; Nouranian, S. Molecular simulation of pH-dependent diffusion, loading, and release of doxorubicin in graphene and graphene oxide drug delivery systems. *J. Mater. Chem. B* **2016**, *4*, 7441–7451.
- [59] Zhao, Q. Q.; Gao, H. S.; Su, Y.; Huang, T. H.; Lu, J. H.; Yu, H.; Ouyang, D. F. Experimental characterization and molecular dynamic simulation of ketoprofen-cyclodextrin complexes. *Chem. Phys. Lett.* **2019**, *736*, 136802.
- [60] DrugBank. *BVZ Sequences* [Online]. <https://go.drugbank.com/drugs/DB00112>.
- [61] Pozzi, D.; Caracciolo, G.; Digiaco, L.; Colapicchioni, V.; Palchetti, S.; Capriotti, A. L.; Cavaliere, C.; Zenezini Chiozzi, R.; Puglisi, A.; Laganà, A. The biomolecular corona of nanoparticles in circulating biological media. *Nanoscale* **2015**, *7*, 13958–13966.
- [62] Mumtaz Virk, M.; Reimhult, E. Phospholipase A₂-induced degradation and release from lipid-containing polymersomes. *Langmuir* **2018**, *34*, 395–405.
- [63] Harada, H.; Takahashi, M. CD44-dependent intracellular and extracellular catabolism of hyaluronic acid by hyaluronidase-1 and -2. *J. Biol. Chem.* **2007**, *282*, 5597–5607.
- [64] Laye, J. P.; Gill, J. H. Phospholipase A₂ expression in tumours: A target for therapeutic intervention. *Drug Discov. Today* **2003**, *8*, 710–716.
- [65] ISO. *Biological evaluation of medical devices - Part 5: Tests for in vitro cytotoxicity (ISO 10993-5:2009)*. International Organization for Standardization: Geneva, 2009.
- [66] Crecente-Campo, J.; Guerra-Varela, J.; Peleteiro, M.; Gutiérrez-Lovera, C.; Fernández-Mariño, I.; Diéguez-Docampo, A.; González-Fernández, Á.; Sánchez, L.; Alonso, M. J. The size and composition of polymeric nanocapsules dictate their interaction with macrophages and biodistribution in zebrafish. *J. Control. Release* **2019**, *308*, 98–108.
- [67] Walkey, C. D.; Olsen, J. B.; Guo, H. B.; Emili, A.; Chan, W. C. W. Nanoparticle size and surface chemistry determine serum protein adsorption and macrophage uptake. *J. Am. Chem. Soc.* **2012**, *134*, 2139–2147.
- [68] Snipstad, S.; Hak, S.; Baghirov, H.; Sulheim, E.; Mørch, Y.; Lélou, S.; von Haartman, E.; Bäck, M.; Nilsson, K. P. R.; Klymchenko, A. S. et al. Labeling nanoparticles: Dye leakage and altered cellular uptake. *Cytometry Part A* **2017**, *91*, 760–766.
- [69] Neuwelt, A. J.; Kimball, A. K.; Johnson, A. M.; Arnold, B. W.; Bullock, B. L.; Kaspar, R. E.; Kleczko, E. K.; Kwak, J. W.; Wu, M. H.; Heasley, L. E. et al. Cancer cell-intrinsic expression of MHC II in lung cancer cell lines is actively restricted by MEK/ERK signaling

- and epigenetic mechanisms. *J. Immunother. Cancer* **2020**, *8*, e000441.
- [70] Marroquin, C. E.; Downey, L.; Guo, H. T.; Kuo, P. C. Osteopontin increases CD44 expression and cell adhesion in RAW 264.7 murine leukemia cells. *Immunol. Lett.* **2004**, *95*, 109–112.
- [71] Krejcová, D.; Pekarova, M.; Safrankova, B.; Kubala, L. The effect of different molecular weight hyaluronan on macrophage physiology. *Neuro Endocrinol. Lett.* **2009**, *30 Suppl 1*, 106–111.
- [72] Qhattal, H. S. S.; Liu, X. L. Characterization of CD44-mediated cancer cell uptake and intracellular distribution of hyaluronan-grafted liposomes. *Mol. Pharm.* **2011**, *8*, 1233–1246.
- [73] Li, W. H.; Yi, X. L.; Liu, X.; Zhang, Z. R.; Fu, Y.; Gong, T. Hyaluronic acid ion-pairing nanoparticles for targeted tumor therapy. *J. Control. Release* **2016**, *225*, 170–182.
- [74] Younis, M. A.; Tawfeek, H. M.; Abdellatif, A. A. H.; Abdel-Aleem, J. A.; Harashima, H. Clinical translation of nanomedicines: Challenges, opportunities, and keys. *Adv. Drug Deliv. Rev.* **2022**, *181*, 114083.
- [75] Dormont, F.; Rouquette, M.; Mahatsekake, C.; Gobeaux, F.; Peramo, A.; Brusini, R.; Calet, S.; Testard, F.; Lepetre-Mouelhi, S.; Desmaële, D. et al. Translation of nanomedicines from lab to industrial scale synthesis: The case of squalene-adenosine nanoparticles. *J. Control. Release* **2019**, *307*, 302–314.
- [76] Valencia, P. M.; Farokhzad, O. C.; Karnik, R.; Langer, R. Microfluidic technologies for accelerating the clinical translation of nanoparticles. *Nat. Nanotechnol.* **2012**, *7*, 623–629.
- [77] FDA. *Q1A(R2) Stability Testing of New Drug Substances and Products* [Online]. 2003. <https://www.fda.gov/regulatory-information/search-fda-guidance-documents/q1ar2-stability-testing-new-drug-substances-and-products>.
- [78] Kampinga, J.; Colaco, C. Compositions for use in rehydration and nutrition during athletic exercise and methods of making same. U.S. Patent 6,596,702, July 22, 2003.
- [79] Van Der Spoel, D.; Lindahl, E.; Hess, B.; Groenhof, G.; Mark, A. E.; Berendsen, H. J. C. GROMACS: Fast, flexible, and free. *J. Comput. Chem.* **2005**, *26*, 1701–1718.
- [80] Schmid, N.; Eichenberger, A. P.; Choutko, A.; Riniker, S.; Winger, M.; Mark, A. E.; van Gunsteren, W. F. Definition and testing of the GROMOS force-field versions 54A7 and 54B7. *Eur. Biophys. J.* **2011**, *40*, 843–856.
- [81] Lu, T. *Sobtop: A Tool of Generating Forcefield Parameters and GROMACS Topology File* [Online]. <http://sobereva.com/soft/Sobtop>.
- [82] Frisch, M. J.; Trucks, G. W.; Schlegel, H. B.; Scuseria, G. E.; Robb, M. A.; Cheeseman, J. R.; Scalmani, G.; Barone, V.; Petersson, G. A.; Nakatsuji, H. et al. *Gaussian 09, Revision B.01*. Gaussian, Inc.: Wallingford, 2010.
- [83] Stephens, P. J.; Devlin, F. J.; Chabalowski, C. F.; Frisch, M. J. *Ab initio* calculation of vibrational absorption and circular dichroism spectra using density functional force fields. *J. Phys. Chem.* **1994**, *98*, 11623–11627.
- [84] Lu, T.; Chen, F. W. Multiwfn: A multifunctional wavefunction analyzer. *J. Comput. Chem.* **2012**, *33*, 580–592.
- [85] O’Boyle, N. M.; Banck, M.; James, C. A.; Morley, C.; Vandermeersch, T.; Hutchison, G. R. Open babel: An open chemical toolbox. *J. Cheminform.* **2011**, *3*, 33.
- [86] Piaggi, P. M.; Parrinello, M. Predicting polymorphism in molecular crystals using orientational entropy. *Proc. Natl. Acad. Sci. USA* **2018**, *115*, 10251–10256.
- [87] Bussi, G.; Donadio, D.; Parrinello, M. Canonical sampling through velocity rescaling. *J. Chem. Phys.* **2007**, *126*, 014101.
- [88] Darden, T.; York, D.; Pedersen, L. Particle mesh Ewald: An $N \log(N)$ method for Ewald sums in large systems. *J. Chem. Phys.* **1993**, *98*, 10089–10092.
- [89] Humphrey, W.; Dalke, A.; Schulten, K. VMD: Visual molecular dynamics. *J. Mol. Graph.* **1996**, *14*, 33–38.
- [90] Grace [Online]. <https://plasma-gate.weizmann.ac.il/Grace/>.